Quantitative characterization of viscoelastic fracture induced by time-dependent intratumoral pressure in a 3D model tumor

View Online   Export Citation   CrossMark

Quang D. Tran,[1,a)] (iD) Marcos,[1,b)] (iD) and David Gonzalez-Rodriguez[2,c)] (iD)

AFFILIATIONS

[1]School of Mechanical and Aerospace Engineering, Nanyang Technological University, Singapore 639798
[2]LCP-A2MC, Institut Jean Barriol, Université de Lorraine, 57070 Metz, France

[a)]**Present address:** Institut de Physique de Nice (INPHYNI), Université Côte d'Azur, CNRS UMR 7010, 06108 Nice, France.
[b)]**Electronic mail:** marcos@ntu.edu.sg
[c)]**Electronic mail:** david.gr@univ-lorraine.fr

ABSTRACT

In the tumor environment, interstitial pressure drives interstitial flow drainage from the tumor core to the lymphatic vessels. Recent studies have highlighted the key role of interstitial pressure in tumor development and cell migration. High intratumoral pressures, up to 60 mm Hg, have been reported in cancer patients. In a previous study, we showed that such pressure levels induce fracture in an experimental tumor model consisting of a microfluidic system holding a cellular aggregate. Here, we investigate and quantify the characteristics of tumor model fracture under a range of flow conditions. Our findings suggest a strong dependence of viscoelastic fracture behavior on the loading rate exerted by flow. The aggregate exhibits fragile fracture at high loading rates and ductile fracture at lower rates. The loading rate also modifies the permeability of the cellular aggregate, as well as the persistence time of the load required to induce fracture. The quantification parameters we propose here, evaluated for an *in vitro* model tumor without the extracellular matrix, could be applied to characterize tumor fracture under more realistic interstitial flow conditions.

I. INTRODUCTION

Metastasis is a complex process involving a massive spread of cancer cells from a primary malignant tumor to multiple sites in the human body.[1] Tumor growth, enabled by anomalous tumor cell proliferation, relies on tumor angiogenesis,[2] the generation of an intratumoral vascular system that provides tumor cells with nutrients. Tumor angiogenesis typically results in a disorganized and leaky vasculature, which enhances leakage from arterial blood capillaries to the tumor environment due to the difference in hydrostatic and osmotic pressures. Part of the fluid returns to the venules, which results in interstitial flow from the arterioles and capillaries to the venules.[3] This flow is insufficient to restore normal pressure values, leading to elevated interstitial fluid pressures at the tumor core.[4] Moreover, the development of new lymphatic vessels in the tumor, known as lymphangiogenesis,[5] is minor and does not match the massive blood vessel development

provided by angiogenesis.[6] This results in significant high interstitial flow out of the tumor to eventually drain into the lymphatic system surrounding it [see Fig. 1(a)]. This directional interstitial flow becomes the essential transporter of both nutrients and signaling molecules to cancer cells and their surrounding environment.[3,7]

Because of its very low velocity (from 0.1 to $4 \mu m\,s^{-1}$),[8,9] the dominant mechanisms by which interstitial flow acts on tumor cells are assumed to be advection and diffusion, rather than flow shear.[3,7,10] However, whereas interstitial flow velocity is low, its driving pressure is high. Measures conducted in human patients' tumors[11–15] demonstrated the existence of pressures of up to 60 mm Hg (or 8000 Pa).[14,16] Our previous work[17] showed that an intratumoral pressure difference higher than 500 Pa applied on a millimetric 3D cellular aggregate, an *in vitro* tumor model, caused aggregate deformation, permeabilization, and fracture. Such fracture triggers a massive detachment of cells from the tumor, which may
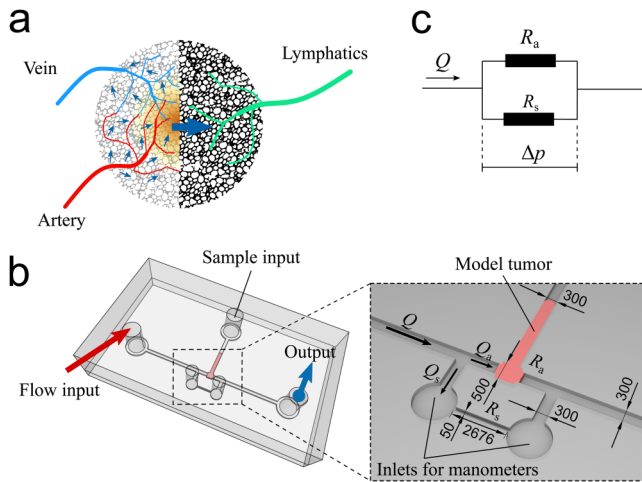
FIG. 1. Strategy and design of our microfluidic system to apply the interstitial fluid pressure on a 3D cellular aggregate modeling a tumor. (a) The diagram illustrates the generation of an elevated interstitial fluid pressure inside a tumor due to the coupling of massive angiogenesis and insufficient lymphangiogenesis. This results in an interstitial flow from the tumor core toward the tumor periphery where lymphatic vessels are present. The blue arrows indicate the interstitial flow resulting from pressure differences between the arteriole and the venule, and between blood and lymphatic vessels. (b) The microfluidic system for cellular aggregate assays with the additional side channel in parallel with the sample chamber. Dimensions are in micrometers. (c) A conceptualization of the microfluidic design represented by analogy with a two-parallel-resistor electrical circuit.

lead to metastasis initiation. Recently, Huang et al.[18] also observed that tumor spheroids seeded within the collagen gel scaffold inside a microfluidic device "exploded" under interstitial flow, which provides evidence that fracture can occur even within the extracellular matrix. Thus, understanding and characterizing tumor fracture under flow will shed light on a potentially important and largely unexplored mechanism of the metastasis initiation.

In this article, we present a detailed characterization of fracture in a 3D model tumor, based on multiple microfluidic assays under various interstitial flow conditions. Our study was conducted using cellular aggregates, which are a well-established *in vitro* model to study fundamental physical mechanisms that could be extrapolated to real tumors.[19–22] Aggregates were placed inside a specifically designed microfluidic device that allows applying a controlled flow while simultaneously measuring the time-evolution of the applied pressure and imaging aggregate deformation.

II. METHODOLOGY

A. Microfluidic design

Our microfluidic design aims to mimic the increased interstitial fluid pressure at the tumor core and the outward force that it exerts onto a section of a tumor [Fig. 1(a)]. Here, the increased pressure is mimicked by imposing a value of the flow rate at the flow inlet. Flow traverses a chamber designed to house a biological

sample, which may contain a cellular aggregate or a collagen gel scaffold, and exits through the flow outlet. An auxiliary channel, labeled "sample input," is needed to introduce the biological sample into the chamber. Two additional channels upstream and downstream of the chamber are connected to two manometers to measure the flow-induced pressure drop. We developed two design variations for the chamber applicable to two types of *in vitro* tumor assays: (1) hydrogel assays, where cells are suspended in a hydrogel solution that is injected into the chamber and then gelified to create a scaffold for the cells;[23–29] (2) cellular aggregate assays, where cellular aggregate spheroids behaving like living viscoelastic droplets[30,31] are fabricated and then pushed into the chamber.[17] For hydrogel assays, we have a design consisting of 5 microchannels radially linked to a rectangular cuboid chamber [Fig. S1(a) in the supplementary material]. This design is appropriate for high permeability samples such as hydrogels but not optimal for low permeability samples such as multicellular spheroids (see the supplementary material for details on the design of hydrogels). Moreover, the pressure developed in the closed input channel upstream, due to flow infusion by the syringe pump, cannot be easily relieved. The setup thus yields rapidly increasing upstream pressures that are difficult to control and that often generate experimental artifacts. The setup thus proved inadequate for our cell aggregate experiments, where we needed to precisely control the rate of pressure difference increase and where we wished to investigate both low and high rates of pressure difference variation. For cellular aggregate assays, we develop another design featuring a narrow side channel in parallel with the sample chamber [Fig. 1(b)]. The input and output channels remain connected through this side channel, which helps to regulate the pressure rise induced by very low permeability samples, such as our cellular aggregates before fracture occurs. Because the hydrodynamic resistance of the side channel R_s is known, this design allows modulating the pressure difference Δp applied to the aggregate in the chamber by varying the total input flow rate Q driven by a programmable syringe pump (KDS Legato 210P, KD Scientific, MA, USA) with a response time of seconds. At the two ends of the side channel, we connect two digital manometers (HD 755-0.5 psi, Extech Instrument, MA, USA) to record the evolution of Δp over time. The hydrodynamics of our setup can be illustrated by an analogy with a simple electric circuit of two resistors in parallel [Fig. 1(c)]. For our design's dimensions, we performed a calibration assay to measure the side channel hydrodynamic resistance of $R_s = 32.18 \pm 0.13 \, \text{Pa min} \mu l^{-1}$ (standard deviation, $N = 5$) for a flow of Dulbecco's Modified Eagle Medium (DMEM) culture medium at 37 °C (Fig. S2(a) in the supplementary material) going through the side channel while the sample chamber is completely blocked. Device dimensions are summarized in Fig. 1(b). In another test, we assessed the ability of our system to generate a step-by-step variation of Δp (Fig. S2(b) in the supplementary material), which is applicable to *in vitro* assays that require a complex time-dependent pressure input.

B. Device fabrication

We fabricate our microfluidic devices with a vertical thickness of 110 μm in Polydimethylsiloxane (PDMS) (Sylgard 184, Dow Chemical, Midland, MI, USA) by a standard soft-lithography

technique.[17,32–35] First, the master mold is fabricated by photolithography with SU-8 2100 to achieve ~110 μm thickness. Then, we mold the master in the PDMS solution with the curing agent at a ratio of 10:1. The PDMS chips are cured for 4 h in an oven at 70 °C, and then bonded to glass slides by a plasma cleaner (Harrick Plasma PDC-001, Ithaca, NY). Right after the plasma bonding, the devices are coated with the fibronectin solution (F1411, Sigma-Aldrich, St. Louis, MO) at a concentration of 100 μg ml^{-1} and incubated at 25 °C for at least 4 h. This coating enables a strong adhesion between cells and channel walls.

C. Cellular aggregate production and experimental preparation

We produce cellular aggregates using the orbital shaking technique[17,36,37] from MCF-7 breast cancer cells (HTB-22, ATCC, Manassas, VA). Cells are cultured in 89% DMEM (cat. 10569-010, ThermoFisher), supplemented with 10% fetal bovine serum (cat. 10270-106, ThermoFisher), and 1% penicillin-streptomycin (cat. 15140-148, ThermoFisher), and they are kept in an incubator (Heracell VIOS 160i, ThermoFisher) at 37 °C and 5% CO_2. When the cultured cells become confluent, we trypsinize and suspend them in 5 ml of fresh CO_2-equilibrated culture medium. A suspension to a final concentration of 4×10^5 cell ml^{-1} is prepared in a small Erlenmeyer flask. We place the flask inside an incubated shaker (LM-420D, Yihder Technology, Xinbei City, Taiwan) spinning at 70 rpm and 37 °C for 20 h. With this setting, we produce spheroidal cellular aggregates ranging from 50 to 500 μm in diameter.

For each experiment, we select one cellular aggregate spheroid with a size between 200 and 400 μm, similar to our previous study[17] (note that multicellular spheroids used in Ref. 17 were also larger than 200 μm, and not larger than 400 μm, as mistakenly stated in this earlier publication). We avoid larger aggregates because they contain dead cells at their core due to the lack of nutrients. The spheroid is introduced into the sample inlet by a micropipette, then pushed to the sample chamber by the periodical compression method.[17] Behaving as a viscoelastic drop, the cellular aggregate deforms and squeezes through the sample input channel, to adopt a flattened shape and fill the sample chamber. The cellular aggregate is then kept in CO_2-equilibrated culture medium at 37 °C under no flow. This resting stage lasts for 2 h to let the cellular aggregate firmly adhere to the channel walls[38] and attain an equilibrium shape. The cell-wall adhesion is very important in this study. In the previous study,[17] we have reported that failure in cell-wall adhesion would result in the cellular aggregate being washed off the sample chamber very fast (see the supplementary material of Ref. 17). Thus, fracture would not be achieved.

III. RESULTS AND DISCUSSION

A. Cellular aggregate's behavior under increasing interstitial pressure

Each experimental run started with $\Delta p = 0$. Q was increased from 0 at a constant flow loading rate, $\dot{Q}$. Figure 2(a) shows an example of a cellular aggregate first deforming and then fracturing under $\dot{Q} = 1.0\,\mu$l min^{-2} [see the supplementary material (Movie 1)
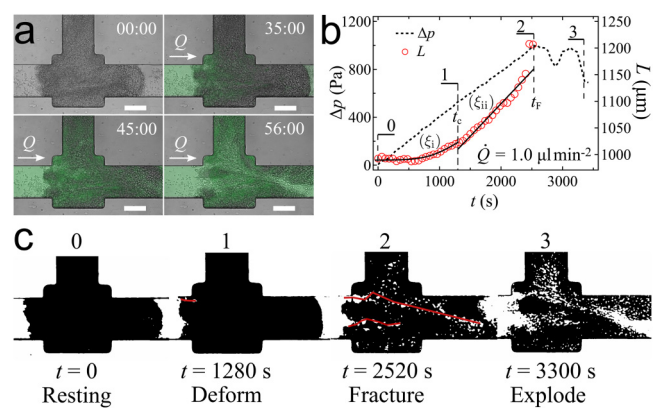

FIG. 2. Fracture of cellular aggregate under increasing interstitial fluid pressure. (a) Images from our microfluidic assay showing a cellular aggregate's deformation and fracture where Q starts from 0 with a loading rate $\dot{Q} = 1.0\,\mu$l min^{-2}. Fluid flows from left to right. Scale bar: 200 μm. (b) The recorded pressure difference Δp linearly increases until a sudden drop happens at $\Delta p_c = 1000$ Pa and $t_F = 2580$ s indicating fracture. The aggregate length L increases from $L_0 \approx 1000\,\mu$m to the maximum length at fracture $L \approx 1200\,\mu$m. During pressure increase, the cellular aggregate deforms as a viscoelastic material following two regimes: (ξ_i) primary creeping with a deformation described by $\varepsilon_i = 4 \times 10^{-8}\,t^2$, and ($\xi_{ii}$) secondary creeping with $\varepsilon_{ii} = 1.3 \times 10^{-4}\,(t - 1280)$. (c) Processed images of the cellular aggregate deforming and fracturing under $\dot{Q} = 1.0\,\mu$l min^{-2}.

for the full experimental run]. We jointly plot the recorded pressure difference Δp and the aggregate length L in Fig. 2(b) to analyze how the aggregate deforms over time. L was retrieved from images of the aggregate shape over time using Fiji.[17,39] We repeated the experiment with different values of $\dot{Q}$ and observed a viscoelastic behavior of cellular aggregates, consistent with previous findings.[17,20,37] The behavior of a cellular aggregate under increasing interstitial pressure can be described as a 3-stage sequence: "deform," "fracture," and "explode" [Fig. 2(c)].

Deform. Starting from the resting state at $\Delta p = 0$, the increase of Δp induced aggregate deformation. During this stage, we observed cracks progressing inside the aggregate. We retrieved images of the crack pathways by image processing with Fiji [Fig. 2(c0-1)]. The processed images had been obtained from raw images by applying a bandpass filter which only retains features larger than the size of a single cell. Then, the crack pathways were drawn and analyzed using MTrackJ[40] [see the supplementary material (Movie 2) for an example of processed images of fracture pathways developed in a cellular aggregate under $\dot{Q} = 0.8\,\mu$l min^{-2}]. The details of the image analysis procedure are presented in the supplementary material.

Fracture. Upon reaching a critical pressure (Δp_c), aggregate fracture occurred. Fracture corresponds to one or multiple visible cracks spanning the aggregate length [Fig. 2(c2)], and it was also signaled by a sudden drop of Δp [Fig. 2(b2)]. The time when fracture occurred is defined as t_F, which is a relevant quantifier of aggregate fracture.

Explode. Fracture led to severe damage to the cellular aggregate structure. A marked drop of Δp signals the fracture event. The resulting increase in interstitial flow through fracture pathways

rapidly enlarged the cracks, disassembled large regions of the aggregate, and eventually washed away big portions of it. We call this aggregate disassembling process "aggregate explosion" [Fig. 2(c3)].

B. Viscoelastic model of cellular aggregate under time-dependent pressure

Previous studies[17,20,31] described the viscoelastic behavior of a cellular aggregate by Zener's model consisting of an elastic spring in parallel with a series of another spring and a damper [Fig. 3(a)]. The pressure difference Δp applied to the aggregate causes it to deform with a strain $\varepsilon(t) = (L(t) - L_0)/L_0$ following the relation

$$\Delta p(t) = E_2 \varepsilon + \eta \frac{E_1 + E_2}{E_1} \dot{\varepsilon}, \tag{1}$$

where $\dot{\varepsilon}$ is the strain rate, and the parameters $E_1 = 4300\,\text{Pa}$, $E_2 = 1750\,\text{Pa}$, $\eta = 1.6 \times 10^6\,\text{Pa s}$ were experimentally obtained previously.[17] If we assume $R_a \gg R_s$, then $\Delta p \approx R_s \dot{Q} t$. Under this hypothesis, the solution to Eq. (1) is

$$\varepsilon(t) = \frac{R_s \dot{Q}}{E_2} \left[t - \eta \frac{E_1 + E_2}{E_1 E_2} \left(1 - e^{-\frac{E_1 E_2 t}{\eta(E_1+E_2)}} \right) \right]. \tag{2}$$

This solution suggests the existence of a characteristic time $t_c = \frac{\eta(E_1+E_2)}{E_1 E_2} \approx 1280\,\text{s}$, which separates two viscoelastic deformation regimes [illustrated in Fig. 2(b)].
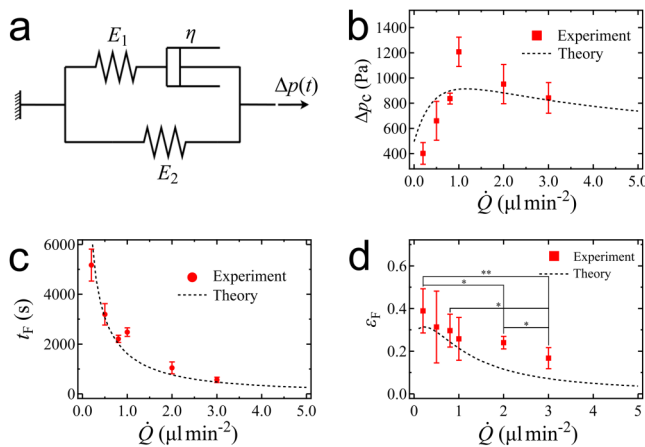

FIG. 3. Parameters showing the viscoelastic behaviors of cellular aggregate under increasing interstitial pressure. (a) Zener model with two springs and one damper to represent cellular aggregate viscoelasticity. (b) Dependence of the critical pressure to induce aggregate fracture Δp_c on the loading rate $\dot{Q}$. (c) Duration t_F needed for the interstitial pressure to induce fracture on a cellular aggregate under different $\dot{Q}$. (d) Aggregate strain at fracture ε_F under different $\dot{Q}$. At $\dot{Q} < 1.0\,\mu\text{l min}^{-2}$, ε_F variations with the flow rate are not significant. When $\dot{Q} > 1.0\,\mu\text{l min}^{-2}$, ε_F significantly decreases with increasing loading rate. The p-values (*$p < 0.05$, **$p < 0.01$) are calculated using the two-sample t-test.

(i) At the short-time limit, where $t \ll t_c$, we have the primary creeping with

$$\varepsilon_i \approx \frac{R_s \dot{Q} E_1}{2\eta(E_1 + E_2)} t^2, \tag{3}$$

showing a quadratic variation of the aggregate strain over time,

(ii) at the long-time limit, where $t \gg t_c$, we have the secondary creeping with

$$\varepsilon_{ii} \approx \frac{R_s \dot{Q}}{E_2} (t - t_c), \tag{4}$$

which indicates a linear deformation of the aggregate over time.

We also see that the rate of increase of aggregate strain is proportional to the loading rate $\dot{Q}$ and thus sensitive to it.

C. Fracture characterization under different flow loading rates

1. Fracture energy and critical pressure

From the physics of adhesion, we know that fracture occurs when a certain amount work has been applied to the system and thus corresponds to a critical energy. It is however more common to report a critical force (or a critical pressure) in experiments, because in many systems, there is an equivalence between the critical energy and the critical force, as we discuss here for the case of aggregate fracture. The work exerted on the aggregate by the interstitial pressure over the time required to fracture, t_F, is $G \equiv \int_0^{t_F} \Delta p \, dL(t)$. By substituting Eq. (1) into G, we obtain

$$G = L_0 E_2 \varepsilon_F^2 \approx \frac{L_0}{2E_2} \Delta p_c^2, \tag{5}$$

where $L_0 \approx 500\,\mu\text{m}$ is the initial length of the cellular aggregate and ε_F is the aggregate strain at fracture. We can estimate the latter by using Eq. (4) to write $\varepsilon_F \approx \Delta p_c / E_2$, where Δp_c is the critical pressure difference that induces aggregate fracture. Thus, the critical pressure depends on $\dot{Q}$ as follows:

$$\Delta p_c(\dot{Q}) = \sqrt{\frac{2E_2 G}{L_0}}. \tag{6}$$

We previously showed[17] that fracture energy G depends on the loading rate $\dot{Q}$ in a way similar to that described for polymers.[41] Introducing this expression for G into Eq. (6), we theoretically predict Δp_c compared to our experimental data in Fig. 3(b). The dependence of Δp_c on $\dot{Q}$ has an identical shape to that of the fracture energy G, which was discussed in our previous work.[17] Thus, aggregate fracture can be described either in terms of a critical energy, which has a direct physical interpretation, or in terms of a critical pressure, which is usually a more straightforward measurement. We emphasize that the whole range of fracture pressures in Fig. 3(b) can be reached in *in vivo* tumors, where pressures as high as 8000 Pa have been recorded,[14,16] which supports the physiological relevance of our study.

2. Time to fracture

Here, we investigate the time needed for the aggregate fracture to happen (t_F) as a function of the loading rate $\dot{Q}$. Figure 3(c) shows that t_F decreases as $\dot{Q}$ increases in experiment. Considering that Δp is built up due to flow limitation by the side channel, i.e., if we assume $R_a \gg R_s$, we can write $\Delta p_c \approx R_s \dot{Q} t_F$. Combining this with Eq. (6), we obtain the following relationship between t_F and $\dot{Q}$:

$$t_F = \sqrt{\frac{E_2 G}{L_0}} \frac{1}{R_s \dot{Q}}. \tag{7}$$

With the expression of G from the previous study,[17] we plot our predicted t_F as a function of $\dot{Q}$ in Fig. 3(c), showing very good agreement with the experimental data. We note that when $\dot{Q} > 2.0\,\mu l\,min^{-2}$, $t_F < t_c$, which implies that for such high loading rates, cellular aggregates only undergo primary creeping as described by Eq. (3). This theoretical model of t_F indicates that a very low flow loading rate results in aggregate fracture at the lowest critical pressure $\Delta p_c \approx 500\,Pa$; however, it requires a duration of ~1.5 h to fracture. This could illustrate a possibility for a tumor to fracture and initiate metastasis even under a slowly increasing intratumoral pressure. In the cases of high loading rates, the pressure builds up very fast and fracture might happen over durations of minutes.

3. Aggregate strain at fracture

Next, we quantify maximum aggregate deformation right before fracture. With t_F given by Eq. (7), we predict aggregate strain at fracture, ε_F, by Eq. (2). As shown in Fig. 3(d), this prediction qualitatively agrees with the experimental data, which shows that the aggregate deformed less as $\dot{Q}$ increases. Specifically, the experimental difference of ε_F between low loading rates ranging from 0.2 to $1.0\,\mu l\,min^{-2}$ is insignificant (p-value, $p > 0.05$). However, the strain significantly decreases at high loading rates, from 0.2 to $3.0\,\mu l\,min^{-2}$ ($p < 0.01$) and from 0.8 to $1.0\,\mu l\,min^{-2}$ ($p < 0.05$). The fast increasing pressure made the aggregate fracture in a short period of time where the maximum aggregate deformation was limited by its viscosity. We note that, at $\dot{Q} = 2.0$ and $3.0\,\mu l\,min^{-2}$, the experimental data of ε_F are higher than the values of the viscoelastic model. We hypothesize that this discrepancy may arise from aggregate architecture disassembly and rearrangement under high loading rates, which could be interpreted as the aggregate deforming over the elastic limit and behaving as a plastic material.

4. Fracture pathways

We collect images of the fracture pathways under different $\dot{Q}$ [see Fig. 4(a)] and quantify pathway curvature by its tortuosity $T = \zeta/C$, where ζ is the total curvilinear length of a pathway, and C the straight-line distance between its two ends. Due to the directionality of the pressure gradient, the tortuosity values at fracture (T_f) indicate rather straight fracture pathways regardless of the loading rate $\dot{Q}$ [see Fig. 4(b)]. We present the tortuosity data in the supplementary material (Table S1). The tortuosity at $\dot{Q} < 0.5\,\mu l\,min^{-2}$ appears to be slightly larger on average than that at higher $\dot{Q}$, even if this experimental result is not significant due to the large standard deviations. This suggested that the increase of
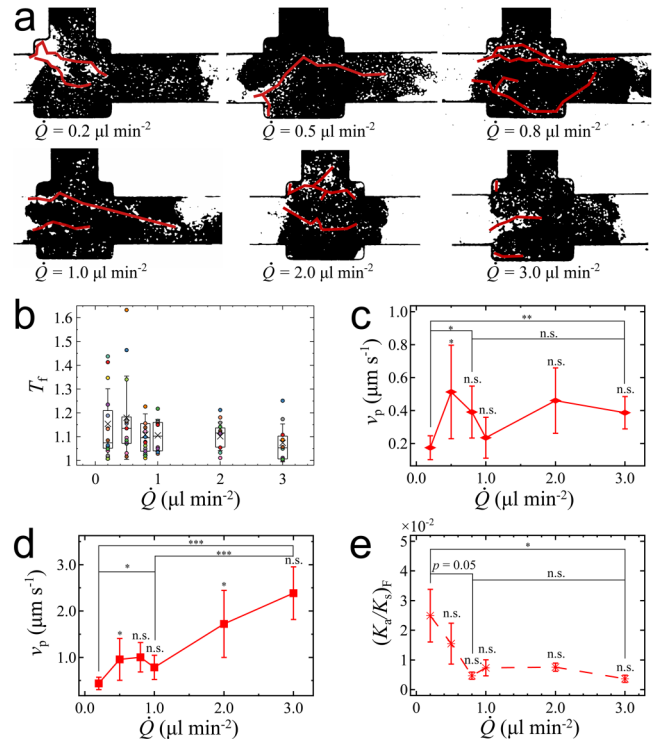

FIG. 4. Characteristics of the fracture pathways. (a) Shapes of fracture pathways under different $\dot{Q}$. (b) Tortuosity at fracture T_f for different $\dot{Q}$ presented by box plot with overlaid data points. The box plot indicates means, quartiles, and standard deviations. Differences of fracture tortuosity for different $\dot{Q}$ are insignificant ($p > 0.05$). (c) Average velocity of fracture pathway growth during the "deform" stage and (d) during the "explode" stage for different $\dot{Q}$. (e) Aggregate permeability at fracture as a function $\dot{Q}$. Each value of $\dot{Q}$ corresponds to $N = 5$ experiment runs using different cellular aggregates. Error bars are standard deviations. The p-values ($*p < 0.05$, $**p < 0.01$, $***p < 0.001$) are calculated from the two-sample t-test.

tortuosity with decreasing $\dot{Q}$ can be explained from the larger deformation of the aggregate at lower loading rates. Due to high aggregate stretching along the flow direction, cell-cell adhesions are weakened, particularly across the flow direction. This would result in more randomly oriented fracture pathways, consistent with both a higher value of the average tortuosity and of its standard deviation.

We next investigate the pathway velocity v_p, which we define as the average one-dimensional growth, measured along the main channel, of all the fracture pathways, i.e., $v_p = \sum \Delta x / (n \Delta t)$, where $\sum \Delta x$ is the total growth along the channel direction of n pathways over a time Δt. In Figs. 4(c) and 4(d), we report two values of v_p for each $\dot{Q}$. These are the average pathway velocities during the "deform" stage and during the "explode" stage. Aggregate fracture occurs at the transition between "deform" and "explode" stages. During the "deform" stage, the pathways have not yet reached the full length of the aggregate. In the "explode" stage, all the pathways reach the full aggregate length over a short time, yielding significantly higher values

of the pathway velocity. Our data show that the average velocity of the fracture pathways does not significantly depend on $\dot{Q}$ [Fig. 4(c)] during the "deform" stage. The "explode" velocity, however, significantly increases with increasing $\dot{Q}$ [Fig. 4(d)].

The development of fracture pathways has been studied here in the absence of extra-cellular matrix (ECM). We expect that the eventual presence of ECM will have an effect on fracture pathway development. On the one hand, ECM may provide mechanical resistance against fracture. On the other hand, ECM shielding yields higher interstitial pressure.[10] These opposing effects are relevant to advanced tumors. For instance, cancerous epithelial cells can signal local fibroblasts to form myofibroblasts, which can secrete significant amounts of ECM proteins.[10,42] This stroma-epithelial association is called "desmoplastic reaction" which stiffens the tissues surrounding the tumor[43] but also contributes to the high pressures recorded in vivo, which can be up to one order of magnitude higher than those obtained in our experiments.[14,16] How these effects of ECM modify the fracture phenomenon in advanced tumors is an open question, which can be addressed by future in vitro studies using ECM scaffolds.

5. Permeability of aggregate fracture

During the "deform" stage, the cellular aggregate progressively becomes more permeable due to its deformation. The flow rate going through the aggregate is determined as $Q_a = Q - Q_s$ [see the inset of Fig. 1(b)], and the intrinsic permeability of the cellular aggregate is estimated as $K_a = \mu Q_a L/(A\Delta p)$, with L being the length of the cellular aggregate, A being the cross-sectional area, and μ being the viscosity of the culture medium. Figure 4(e) shows the aggregate's intrinsic permeability K_a in reference with the constant permeability of the side channel right at the time when fracture is reached, as a function of the applied $\dot{Q}$. The constant permeability of the side channel ($K_s = 1.97 \times 10^{-10}$ m^2) is taken as a reference. Note that, after fracture, a big fragment of the aggregate is removed, which makes the calculation no longer valid. We observe that K_a/K_s at fracture, which we note $(K_a/K_s)_F$ is highest for $\dot{Q} = 0.2\,\mu$l min^{-2}. Then, K_a decreases as $\dot{Q}$ increases up to $0.8\,\mu$l min^{-2}. Beyond $0.8\,\mu$l min^{-2}, K_a varies insignificantly around an estimated minimal value of $K_{a,F} = 1.12 \times 10^{-12}$ m^2, which is comparable to the average intrinsic permeability of the collagen gel.[17,27] Converting to hydraulic resistance ratio, we obtain $(R_s/R_a)_F \approx 1$ at $\dot{Q} = 0.2\,\mu$l min^{-2}, and $(R_s/R_a)_F \approx 0.2$ for $\dot{Q} = 0.8$ to $3.0\,\mu$l min^{-2}. Thus, fracture damages cellular aggregates so that their hydrodynamic resistance can become as low as that of the side channel. This is to be compared with the initial aggregate state, when aggregate resistance is much higher than that of the side channel (initial $R_a > 100R_s$). Aggregate fracture damage beyond $(R_s/R_a)_F \approx 1$ may be precluded in our device by the presence of the side channel. In another words, the side channel limits any further damage to the cellular aggregate due to the parallel configuration between the sample chamber and the side channel. As $(R_s/R_a)_F$ increases to 1, the total resistance of the whole system is accordingly reduced by half, causing a drastic decrease of Δp and a balance of flow rates through the side channel and the sample chamber.

IV. CONCLUSION

This study investigates the quantitative characteristics of fracture occurring in a model tumor subjected to increasing interstitial fluid pressure. We study the viscoelastic deformation of the aggregates under interstitial flow and described two regimes: a short-time viscoelastic regime and a long-time elastic regime, followed by fracture once the interstitial pressure becomes high enough. We demonstrate that aggregate fracture can either be quantified by a critical energy or equivalently by a critical pressure. In our system, the flow loading rate of $1.0\,\mu$l min^{-2} results in aggregate fracture at the highest critical pressure of 1200 Pa. Loading rates higher than $1.0\,\mu$l min^{-2} cause fracture at a slightly lower critical pressure. The critical pressure is lowest ($\sim$400 Pa) at very slow loading rates. Our theoretical conceptualization of the aggregate behavior under interstitial pressure successfully explains the observed variations of the time to fracture and of the maximum strain as a function of the loading rate, $\dot{Q}$. The time to fracture increases when $\dot{Q}$ decreases. Our model predicts that a tumor may fracture under a slow but sustained development of intratumoral pressure, which in our experimental system requires a duration longer than an hour. In contrast, high loading rates can result in tumor fracture within minutes. In a real tumor, intratumoral pressure fluctuates over time. Thus, investigations accounting for pressure fluctuations and for the complex tumor environment would be needed in order to extrapolate our results. Aggregate permeability is significantly enhanced by fracture, in a way that depends on the loading rate. Lower $\dot{Q}$ enhances aggregate deformation and fracture damage. Higher $\dot{Q}$ induces a more fragile aggregate behavior. In the latter case, fracture occurs rapidly but fracture damage, as quantified by the resulting permeability, remains more limited. Through the theoretical model, we also learn that changing the size of the input channel or the sample chamber containing the cellular aggregate will affect the fracture energy and critical pressure of the aggregate. However, we expect the viscoelastic parameters such as E_1, E_2, η to only depend on the material of the tumor or the cell-cell adhesion. Thus, our model should be applicable to different aggregate sizes and cell types.

Overall, our studies of fracture in a model tumor indicate that fracture characteristics are very sensitive to temporal variations in interstitial pressure. This is an important result, because intratumoral pressure continuously varies in in vivo conditions, both temporally and spatially, due to blood pressure variations and to the heterogeneity of the complex tumor microenvironment. Moreover, the presence of extra-cellular matrix in advanced tumors is expected to increase mechanical strength but also interstitial pressure, due to the stiffened stroma. It is thus emphasized that our measured parameter values correspond to our in vitro model, and care should be taken when extrapolating these values to in vivo conditions. To narrow the gap between in vitro and in vivo, future studies need to extend the approach presented here to investigate more realistic conditions of interstitial pressure and extra-cellular matrix support, such as by considering periodically varying pressure inputs and by using tumor cells embedded in an ECM scaffold.

SUPPLEMENTARY MATERIAL

See the supplementary material for more information about our microfluidic system for hydrogel assays, calibration of the

devices, image processing procedure, and the experimental data of the fracture pathways' tortuosity. We also present two supplementary movies showing aggregate fracture observe for a loading rate of $1.0\,\mu$l min^{-2} and the development of fracture pathways in the cellular aggregate under a loading rate of $0.8\,\mu$l min^{-2}.

REFERENCES

[1] G. Poste and I. J. Fidler, Nature 283, 139 (1980).

[2] J. Folkman, Semin. Oncol. 29, 15 (2002).

[3] M. A. Swartz and A. W. Lund, Nat. Rev. Cancer 12, 210 (2012).

[4] T. P. Butler, F. H. Grantham, and P. M. Gullino, Cancer Res. 35, 3084 (1975).

[5] M. Dadiani, V. Kalchenko, A. Yosepovich, R. Margalit, Y. Hassid, H. Degani, and D. Seger, Cancer Res. 66, 8037 (2006).

[6] J. Sleeman, A. Schmid, and W. Thiele, Semin. Cancer Biol. 19, 285 (2009).

[7] M. A. Swartz and E. Fleury, Annu. Rev. Biomed. Eng. 9, 229 (2007).

[8] H. Dafni, T. Israely, Z. M. Bhujwalla, L. E. Benjamin, and M. Neeman, Cancer Res. 62, 6731 (2002).

[9] S. R. Chary and R. K. Jain, Proc. Natl. Acad. Sci. U.S.A. 86, 5385 (1989).

[10] A. C. Shieh and M. A. Swartz, Phys. Biol. 8, 015012 (2011).

[11] Y. Boucher, J. M. Kirkwood, D. Opacic, M. Desantis, and R. K. Jain, Cancer Res. 51, 6691 (1991).

[12] J. R. Less, M. C. Posner, Y. Boucher, D. Borochovitz, N. Wolmark, and R. K. Jain, Cancer Res. 52, 6371 (1992).

[13] R. Gutmann, M. Leunig, J. Feyh, A. E. Goetz, K. Messmer, E. Kastenbauer, and R. K. Jain, Cancer Res. 52, 1993 (1992).

[14] B. D. Curti, W. J. Urba, W. G. Alvord, J. E. Janik, J. W. Smith, K. Madara, and D. L. Longo, Cancer Res. 53, 2204 (1993).

[15] S. D. Nathanson and L. Nelson, Ann. Surg. Oncol. 1, 333 (1994).

[16] C.-H. Heldin, K. Rubin, K. Pietras, and A. Östman, Nat. Rev. Cancer 4, 806 (2004).

[17] Q. D. Tran, Marcos, and D. Gonzalez-Rodriguez, Soft Matter 14, 6386 (2018).

[18] Y. L. Huang, Y. Ma, C. Wu, C. Shiau, J. Segall, and M. Wu, in APS March Meeting Abstracts (American Physical Society, 2019), p. K66.002.

[19] W. Mueller-Klieser, J. Cancer Res. Clin. Oncol. 113, 101 (1987).

[20] D. Gonzalez-Rodriguez, L. Bonnemay, J. Elgeti, S. Dufour, D. Cuvelier, and F. Brochard-Wyart, Soft Matter 9, 2282 (2013).

[21] R.-Z. Lin and H.-Y. Chang, J. Biotechnol. 3, 1172 (2008).

[22] G. Beaune, C. Blanch-Mercader, S. Douezan, J. Dumond, D. Gonzalez-Rodriguez, D. Cuvelier, T. Ondarçuhu, P. Sens, S. Dufour, M. P. Murrell et al., Proc. Natl. Acad. Sci. U.S.A. 115, 12926 (2018).

[23] V. Vickerman, J. Blundo, S. Chung, and R. D. Kamm, Lab Chip 8, 1468 (2008).

[24] S. Chung, R. Sudo, P. J. Mack, C.-R. Wan, V. Vickerman, and R. D. Kamm, Lab Chip 9, 269 (2009).

[25] Y. Shin, S. Han, J. S. Jeon, K. Yamamoto, I. K. Zervantonakis, R. Sudo, R. D. Kamm, and S. Chung, Nat. Protoc. 7, 1247 (2012).

[26] I. K. Zervantonakis, S. K. Hughes-Alford, J. L. Charest, J. S. Condeelis, F. B. Gertler, and R. D. Kamm, Proc. Natl. Acad. Sci. U.S.A. 109, 13515 (2012).

[27] W. J. Polacheck, I. K. Zervantonakis, and R. D. Kamm, Cell. Mol. Life Sci. 70, 1335 (2013).

[28] U. Haessler, J. C. Teo, D. Foretay, P. Renaud, and M. A. Swartz, Integr. Biol. 4, 401 (2012).

[29] Y. L. Huang, C.-K. Tung, A. Zheng, B. J. Kim, and M. Wu, Integr. Biol. 7, 1402 (2015).

[30] H. Phillips and M. Steinberg, J. Cell Sci. 30, 1 (1978).

[31] K. Guevorkian, D. Gonzalez-Rodriguez, C. Carlier, S. Dufour, and F. Brochard-Wyart, Proc. Natl. Acad. Sci. U.S.A. 108, 13387 (2011).

[32] G. M. Whitesides, E. Ostuni, S. Takayama, X. Jiang, and D. E. Ingber, Annu. Rev. Biomed. Eng. 3, 335 (2001).

[33] Marcos and R. Stocker, Limnol. Oceanogr. Methods 4, 392 (2006).

[34] Marcos, H. C. Fu, T. R. Powers, and R. Stocker, Phys. Rev. Lett. 102, 158103 (2009).

[35] Q. D. Tran, T. F. Kong, D. Hu, Marcos, and R. H. Lam, Lab Chip 16, 2813 (2016).

[36] P. L. Ryan, R. A. Foty, J. Kohn, and M. S. Steinberg, Proc. Natl. Acad. Sci. U.S.A. 98, 4323 (2001).

[37] K. Guevorkian, M.-J. Colbert, M. Durth, S. Dufour, and F. Brochard-Wyart, Phys. Rev. Lett. 104, 218101 (2010).

[38] S. Douezan, K. Guevorkian, R. Naouar, S. Dufour, D. Cuvelier, and F. Brochard-Wyart, Proc. Natl. Acad. Sci. U.S.A. 108, 7315 (2011).

[39] J. Schindelin, I. Arganda-Carreras, E. Frise, V. Kaynig, M. Longair, T. Pietzsch, S. Preibisch, C. Rueden, S. Saalfeld, B. Schmid et al., Nat. Methods 9, 676 (2012).

[40] E. Meijering, O. Dzyubachyk, and I. Smal, in Methods in Eenzymology (Elsevier, 2012), Vol. 504, pp. 183–200.

[41] F. Saulnier, T. Ondarçuhu, A. Aradian, and E. Raphaël, Macromolecules 37, 1067 (2004).

[42] M. F. Insana, C. Pellot-Barakat, M. Sridhar, and K. K. Lindfors, J. Mammary Gland Biol. Neoplasia 9, 393 (2004).

[43] T. A. Krouskop, T. M. Wheeler, F. Kallel, B. S. Garra, and T. Hall, Ultrason. Imaging 20, 260 (1998).